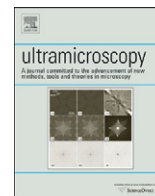




ELSEVIER

Contents lists available at SciVerse ScienceDirect

## Ultramicroscopy

journal homepage: [www.elsevier.com/locate/ultramic](http://www.elsevier.com/locate/ultramic)

## Experimental procedures to mitigate electron beam induced artifacts during *in situ* fluid imaging of nanomaterials

Taylor J. Woehl<sup>a,\*</sup>, Katherine L. Jungjohann<sup>a</sup>, James E. Evans<sup>b,c</sup>, Ilke Arslan<sup>a,c</sup>, William D. Ristenpart<sup>a,d</sup>, Nigel D. Browning<sup>a,b,c</sup>

<sup>a</sup> Department of Chemical Engineering and Materials Science, University of California, Davis, Davis, CA 95616, USA

<sup>b</sup> Department of Molecular and Cellular Biology, University of California, Davis, Davis, CA 95616, USA

<sup>c</sup> Pacific Northwest National Laboratory, Richland, WA 99352, USA

<sup>d</sup> Department of Food Science and Technology, University of California, Davis, Davis, CA 95616, USA

## ARTICLE INFO

Available online 27 July 2012

## Keywords:

*in situ* TEM

*in situ* STEM

*in situ* fluid

*in situ* liquid

## ABSTRACT

Scanning transmission electron microscopy of various fluid and hydrated nanomaterial samples has revealed multiple imaging artifacts and electron beam–fluid interactions. These phenomena include growth of crystals on the fluid stage windows, repulsion of particles from the irradiated area, bubble formation, and the loss of atomic information during prolonged imaging of individual nanoparticles. Here we provide a comprehensive review of these fluid stage artifacts, and we present new experimental evidence that sheds light on their origins in terms of experimental apparatus issues and indirect electron beam sample interactions with the fluid layer. A key finding is that many artifacts are a result of indirect electron beam interactions, such as production of reactive radicals in the water by radiolysis, and the associated crystal growth. The results presented here will provide a methodology for minimizing fluid stage imaging artifacts and acquiring quantitative *in situ* observations of nanomaterial behavior in a liquid environment.

© 2012 Elsevier B.V. All rights reserved.

### 1. Introduction

Fluid stage transmission electron microscopy (TEM) and scanning transmission electron microscopy (STEM) are emerging *in situ* techniques in which nanomaterials, whole cells, and dynamic processes can be imaged in real-time in a fluid environment [1–8]. As with conventional electron microscopy of solid samples, electron beam interactions with both the sample and the surrounding fluid are important to understand, especially since the fluid is a highly mobile environment that can rapidly propagate both physical and chemical damage. To obtain consistency in these emerging fields, a crucial first step is to establish the common artifacts and electron beam interactions that can occur.

A comprehensive study of sample radiation damage in transmission and scanning electron microscopy techniques was provided by Egerton and Malac [9]. The chapters in Analytical Electron Microscopy by Glaeser and Hobbs also have a thorough analysis of radiation damage of soft and hard materials in electron microscopy [10,11]. However, those reviews focused on beam interactions with samples inside the vacuum of the microscope rather than in a fluid environment. Zheng et al. and Fukushima

et al. investigated electron beam–sample interactions in a fluid under TEM illumination, for liquid and gaseous water [5,12]. These interactions included beam heating, direct momentum transfer, sample charging, carbon contamination, and mass loss. Since TEM and STEM have very different modes of illumination, they will cause different beam effects within the fluid sample. Therefore, the challenge remains to establish a list of common artifacts, understand the origins of each artifact, and devise procedures to mitigate the adverse impact of these artifacts during *in situ* fluid STEM and TEM.

The goal of this paper is to provide a comprehensive overview of the artifacts that we have identified to date during *in situ* fluid STEM experiments. Toward that end, the paper is organized as follows (cf. Table 1). We show that artifacts arise from at least three sources: (1) the experimental apparatus (primarily from the silicon nitride (SiN) windows), (2) from indirect interactions between the sample and aqueous chemical species formed by the electron beam, and (3) the direct interaction between the electron beam and the sample. More specifically we discuss the artifacts arising from these sources, including crystal growth, carbon contamination, bubble formation, charging effects on nanoparticles, and loss of atomic information in high resolution images. First, we provide a review of previous observations of artifacts induced during *in situ* fluid STEM and TEM experiments, and we summarize the known mitigation techniques. The origin

\* Corresponding author. Tel.: +1 816 210 1557; fax: +1 530 752 1031.  
E-mail address: [tjwoehl@ucdavis.edu](mailto:tjwoehl@ucdavis.edu) (T.J. Woehl).

**Table 1**  
Summary of the effects of common artifacts on *in situ* fluid STEM experiments, their causes, and solutions to mitigate their effects.

Artifact	Cause	Section	Methods to mitigate
<b>Fluid stage windows and tip</b>			
Large fluid path length, degraded imaging and EELS resolution	Window bulging	1.1.1	Adjust window geometry, add membrane supports
Evaporation of the fluid layer, vacuum degradation in microscope	Incomplete vacuum sealing	1.1.2	Eliminate large particulate matter, low vapor pressure liquid, use designated fluid holders
Liquid void between windows	Dewetting of liquid film	1.1.3 3.1.2	Plasma and glow discharge treatment of windows, excess fluid in well surrounding chips
<b>Sample preparation</b>			
Material deposition in irradiated area causes contrast degradation	Carbon contamination on vacuum or liquid side	3.1.1	Plasma and glow discharge treatment of windows, eliminate carbon species from sample, careful sample handling
<b>Beam-sample interactions</b>			
Rapid growth of nanocrystals on SiN windows inside and outside of irradiated area	Reduction of reactive ions by radicals in solution	1.2.1 1.2.2 3.2.1	Image below electron dose threshold, eliminate reactive species from solution
Repulsion of freely diffusing nanoparticles from irradiated area	Charging of window and particles by electron beam	1 3.3.1	Low dose imaging, deposit a thin conductive film on the window, add electrolyte to screen the charging
Loss of atomic information over time at high magnifications and electron doses	Contamination, atomic rearrangement	1 3.3.2	Low dose imaging techniques, eliminate carbon and crystal contamination precursors from solution

of several of the observed artifacts has remained obscure, so we then describe a series of STEM experiments to illuminate the underlying mechanisms giving rise to these artifacts. A key finding is that many of the artifacts become negligible below a critical electron dose, presumably due to decreased inelastic scattering in the fluid layer. The results should help microscopists to minimize fluid STEM artifacts and to obtain quantitative *in situ* information about the behavior of nanomaterials in a fluid environment.

## 1.1. Experimental apparatus artifacts

### 1.1.1. Window bulging

Window bulging is an issue leading to multiple artifacts in fluid stage experiments, such as microbubble formation, degassing, and decreased resolution by beam broadening and chromatic aberrations [13,14]. Bubble formation is discussed in 3.1.2, we first focus here on the cause of window bulging and potential steps to alleviate its effects. Bulging of the electron transparent windows (typically 50 nm thick amorphous SiN or silicon dioxide) is due to the pressure differential between the hermetically sealed fluid stage and the high vacuum in the sample chamber of the microscope. Ring et al. showed that the fluid path length in the center of the windows can be up to 100% longer than at the edge of the window due to bulging of the membranes [15]. Window bulging has also been shown to degrade the energy resolution of electron energy loss spectroscopy (EELS) in the fluid stage [16]. Increasing the fluid layer thickness past one inelastic mean free path introduces multiple scattering effects and yields low signal-to-noise ratios in EELS spectra. This effect reduces the area in which EELS can be performed to the corners of the SiN membranes, where the bulging is minimal. A potential solution for window bulging was described by Grogan et al., who found that by observing the Newton rings on the fluid filled SiN windows with a stereo microscope, they could extract the approximate amount of bowing and adjust the pressure on the sealing o-rings to reduce the bulging [17]. This is not a universal solution, however, because there is no way of adjusting the pressure on the o-rings in commercial fluid stages. One potential solution would be to add an array of micron sized pillars to the window area, with a height equal to the desired fluid path length, and wafer bond these to the other window. This procedure would effectively eliminate bulging of both windows, by pinning the

surfaces together. Wafer bonding has already been employed for *in situ* fluid platforms by Grogan et al., who used this technique to bond two silicon chips together to form the nano-sized cavity for liquid STEM imaging [17]. Reducing the lateral dimensions, adding grid supports, or wafer bonding the windows are all potential universal solutions for window bulging, yet there have been no reports to date on their application.

### 1.1.2. Sealing issues

An incomplete hermetic seal in the fluid stage enclosure allows evaporation of the liquid between the electron transparent windows [5]. One procedure to lessen this effect is addition of a fluid with a lower vapor pressure than water, such as glycerol, to slow down the rate of fluid evaporation [5,18]. Another approach, pioneered by Gai et al. is environmental TEM (ETEM), a technique in which the sample chamber is kept at a higher pressure than the rest of the column [19]. The wet ETEM technique uses a windowless approach in the sample stage that eliminates both window bulging and sealing issues, although this technique suffers from very large gas/liquid path lengths [19].

### 1.1.3. Surface treatment of fluid stage windows

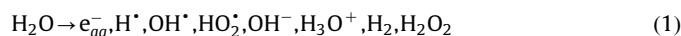
Dewetting of the fluid from the windows is another experimental apparatus issue that can lead to bubble formation and artifacts during imaging. The amorphous SiN membrane on the silicon chips is originally hydrophobic after production, due to surface roughness and a thin layer of organic contaminants on the surface [15]. It is advantageous to have a hydrophilic surface to prevent bubble formation, dewetting of the fluid sample, and also to facilitate attachment of biological cells to the window surface [15]. Ring et al. showed that plasma cleaning and hydrophilic coatings, such as poly-L-lysine, both created a hydrophilic surface that the fluid would wet effectively [15].

## 1.2. Interaction of the electron beam with the fluid

### 1.2.1. Radiolysis of water

It is well established that irradiating water with electrons of incident energies greater than  $\sim 10$  eV (the bond energy of a valence electron in water) creates radical species and aqueous electrons in the fluid, via ionization of water molecules [20]. The effect these species have on imaging during *in situ* fluid STEM,

however, is less well characterized; therefore this discussion will be limited to inelastic scattering of 100–300 keV electrons by liquid water (typical fluid STEM conditions). The primary reaction occurring in an aqueous system irradiated by electrons is the radiolysis of water (1) to create the constituent hydrogen and hydroxide radicals, excited water molecules, and other molecular species [20]:



In addition to these species, inelastic scattering events lead to the creation of hydrated electrons in the water ( $e_{aq}^-$ ) [21]. Aqueous electrons are created when an electron loses sufficient energy through excitation and ionization scattering events to become a subexcitation electron (*i.e.* its energy is smaller than the valence excitation energy of a water molecule ( $< 10$  eV)) [20]. The electron retains its unit negative charge and is then surrounded by a hydration shell, effectively becoming an ionic species [21]. The reaction scheme is



here  $e_{incident}^-$  is an incident electron,  $\text{H}_2\text{O}^+$  is an ionized water molecule,  $e_{sub}^-$  is a subexcitation electron,  $\text{H}_2\text{O}^*$  is an excited water molecule,  $e_{aq}^-$  is an aqueous electron, and  $n\text{H}_2\text{O}$  represents a hydration shell. The subexcitation electron has two paths that it can follow after ionizing a water molecule (2): recombination with the ionized water molecule (3), or thermalization and solvation to form an aqueous electron (4). Caer reported that a total yield of approximately 0.75  $\mu\text{mol}/\text{J}$  of radicals are produced in water (pH 3–11) irradiated with electrons of energies between 0.1 and 10 MeV (100–1000 keV) [22]. The aqueous electron and hydroxide radical have equal yields and make up 75% of the radicals created, while hydrogen radicals (8%), hydrogen gas (6%), hydrogen peroxide (10%), and hydroperoxyl radicals (1%) compose the remaining 25% of the primary radicals produced [22]. The pH of the water also determines the yields of the radicals; for example, water of pH=0.5 irradiated by electrons has a negligible equilibrium yield of aqueous electrons, due to rapid recombination of the electrons with hydrogen ions [22].

Both the hydrogen radical and aqueous electron are strong reducing species that will react with aqueous electronegative ions (*i.e.* soluble transition metals) to form crystals [21]. This reaction has implications for fluid stage studies of reactive fluid samples, because it is likely the mechanism for electron beam induced nanoparticle growth [6,8]. Watanabe and Saito used Monte Carlo simulations to calculate the yields of radical species created by electron irradiation of water [23]. They showed that hydrogen radicals, hydroxide radicals, and aqueous electrons have the highest yield compared to all other species created by the beam. Recently, Caer provided data that suggested secondary electrons formed in pulse electron irradiated silica nanoparticles were transferred to the water and became solvated, yet their respective hole pairs remained trapped in the solid [22]. This will likely lead to an altered yield of aqueous electrons in the fluid stage, as the thin layer of silicon oxide existing on the SiN window surface may facilitate transfer of electrons across the interface. de Jonge et al. have noted that it is advantageous to maintain constant flow through the fluid cell to remove these species by convection, therefore reducing damage to cell tissue and other adverse reactions [7,18]. Another possible remedy to remove aqueous electrons is to add electron scavenging species, such as dissolved

oxygen and hydrogen peroxide, which will react with the electrons before they can cause damage to the sample [21]. Understanding and manipulating the radical chemistry in fluid samples in the electron microscope will be very important in the future to determine the mechanisms involved in electron beam initiated processes, and to alleviate artifacts caused by radical species.

### 1.2.2. Nanocrystal growth experiments and indirect electron beam effects

Indirect electron beam effects refer to secondary effects the electron beam has on a system, such as radiolysis damage [9]. These effects seem to have a significant impact on *in situ* fluid experiments, both in TEM and STEM imaging modes. Zheng et al. recently observed electron beam induced growth of platinum nanoparticles in a 200 nm thick fluid layer [6]. The authors found that irradiating an organic solution containing platinum precursor with a 300 kV TEM beam induced spontaneous growth of platinum nanoparticles in the bulk fluid. Similar beam induced crystal growth, this time using an aqueous solvent, was recently reported by Evans et al. using *in situ* fluid STEM [8]. They observed crystal growth outside of the irradiated area, suggesting that the nanoparticle growth was indirectly caused by the electron beam. The STEM beam has also been shown to have the opposite effect on nanoparticles, as de Jonge et al. noted that gold nanoparticles dissolved in water during high magnification ( $> M=500,000$ ) imaging [13].

Klein et al. showed that at high electron dosages a TEM beam can displace fluid between the two windows, effectively creating a bubble between the fluid stage windows, yet it was not clear whether the beam was vaporizing or hydrolyzing the water [14]. White et al. also found that nanobubbles in water could be manipulated by the STEM beam; where at low magnifications (9.1 and 13 kx), electron irradiation caused the bubble to shrink and eventually collapse, yet at high magnifications (25 kx) the STEM beam caused the bubble to grow [24]. The electron beam has a large effect on *in situ* experiments through indirect channels, with effects ranging from nanocrystal growth to bubble formation and manipulation.

## 2. Materials and methods

Multiple experiments employing various nanoparticle suspensions and reactive aqueous systems were compiled to study the possible imaging artifacts for fluid STEM. In the following section, we describe the synthesis and properties of the various samples and then outline the *in situ* fluid STEM technique and the accompanying procedures for cleaning and loading the SiN windows. Finally, we outline a procedure for performing *post situ* SEM/EDS analysis of the SiN windows.

### 2.1. Nanoparticle synthesis

Gold nanoparticles were grown using a sodium citrate (Sigma-Aldrich, USA) solution reduction of chloroauric acid (Acros Organics, USA) [25]. The synthesized gold nanoparticle solutions were centrifuged and washed with 1 mM potassium chloride (KCl) electrolyte (Fisher Scientific, USA), and then diluted 50 times with 1 mM KCl. The gold nanoparticle suspension had an average size of  $36.47 \pm 22$  nm and an average zeta potential of  $-19.3 \pm 4.9$  mV. (Here the zeta potential refers to the experimentally measured magnitude and sign of the particle surface charge; where a negative zeta potential indicates negative surface charge [26]). Citrate stabilized gold nanoparticles, imaged in Supplementary movie #4, were acquired from Ted Pella (Redding, CA, USA) and had an average particle size of  $21.74 \pm 5.47$  nm and

an average zeta potential of  $-33.9 \pm 2.7$  mV at 100 times dilution in DI water. Titanium dioxide ( $\text{TiO}_2$ ) nanoparticles were obtained from Sigma-Aldrich and had an average crystal size of 21 nm. The  $\text{TiO}_2$  powder was dispersed and diluted 100 times in DI water. Because there was no stabilizing electrolyte added, the  $\text{TiO}_2$  nanoparticles flocculated into aggregates with an average size of  $625 \pm 200$  nm, which had an average zeta potential of  $26.7 \pm 4.9$  mV. Aggregates on the order of 100–200 nm were also observed during *in situ* fluid STEM experiments. The average particle sizes and zeta potentials of the nanoparticles were measured using a dynamic light scattering apparatus (Malvern Instruments Ltd, UK). Constituents of the lead sulfide nanoparticle growth experiments are given in a previous publication [8].  $\text{AgNO}_3$  was obtained from Fisher Scientific and dissolved in water at a concentration of 1 mM.

## 2.2. Fluid stage assembly

We utilized a continuous flow *in situ* fluid stage (Hummingbird Scientific, USA) equipped with a reusable tip. The environmental chamber was formed in the fluid stage tip by sandwiching two  $2.6 \times 2.6$  mm<sup>2</sup> silicon chips, with a  $50 \times 200$   $\mu\text{m}^2$  opening etched from the center. Each chip had a 50 nm thick amorphous SiN membrane that spanned the opening and formed the electron transparent window. Gold spacers, with thicknesses ranging from 50 to 200 nm, were deposited onto the four corners of each chip to form the spacing for the fluid (see [8] for details on processing). Silicon chips of similar design, purchased from Hummingbird Scientific (Lacey, WA, USA), were used for some experiments and did not have gold spacers deposited onto them. For experiments using these chips, 30 nm gold nanoparticles in the solution created the necessary spacing for the fluid layer. A schematic representation of the fluid stage chip assembly is shown in Fig. 1.

Prior to an experiment, the silicon chips were rinsed with DI water and the fluid stage tip was rinsed with ethanol and then DI water. In some cases, plasma cleaning or glow discharge treatment was applied to the windows as well (indicated when used). To load a fluid sample, one chip was placed membrane side up inside the empty fluid stage tip, and a 0.5  $\mu\text{L}$  drop of sample was placed onto the chip with a pipette. Another chip was then placed membrane side down on top of the liquid drop. The windows in the two chips were then aligned under a stereo microscope using a pair of tweezers to adjust their positions. The tip of the fluid stage was then assembled to isolate the fluid sample from the vacuum of the microscope. Prior to inserting the stage into the microscope, it was placed in a dry pumping station (Pfeiffer Vacuum GmbH, Germany) to simulate the vacuum of the microscope, and ensure that the tip of the stage was properly sealed and the SiN windows were intact.

Plasma cleaning of the fluid stage chips was performed in a PDL-32G oxygen plasma cleaner (Harrick Plasma, USA). Glow discharge treatment of the windows was performed using a home-made apparatus. During glow discharge, the windows were

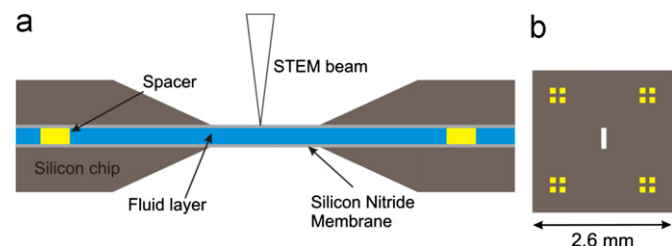


**Fig. 1.** (a) Detailed schematic of the silicon chips used to contain the fluid layer (b) top down schematic of a single silicon chip with gold platform spacers on each corner.

placed SiN membrane side up on a paraffin film covered microscope slide that was then placed between two adjacent electrodes. The apparatus was evacuated to a pressure of  $\sim 1$  mPa using a roughing pump, and a 1 A 110 V DC voltage was applied between the electrodes to create an oxygen plasma in the chamber. Typically, the windows were plasma cleaned for 1 min, 1 h prior to the experiment, to remove any residual carbon from the surfaces and render the windows more hydrophilic. Since the effects of plasma cleaning wore off after 1–2 h, the windows were glow discharged for 30 s immediately before loading the sample.

## 2.3. Scanning transmission electron microscopy

The assembled fluid stage was imaged in a spherical aberration corrected JEOL 2100F/Cs (S)TEM (Fig. 2). The microscope was operated in STEM mode at 200 kV, with a beam current of 0.04 nA. The microscope was first aligned to 2–3 Å resolution with a platinum/iridium standard sample in a single tilt holder. After alignment the holder was removed and the fluid stage inserted into the microscope and imaged. High angle annular dark field (HAADF) ( $\beta = 70$  mrad) and bright field (BF) images, as well as EELS spectra, were collected during imaging of the fluid samples. STEM/EELS was used to confirm the presence of a fluid layer between the windows, which was indicated by a large plasmon peak in the low loss spectra [16]. Fluid layer thicknesses were calculated using the relative log-ratio method in Digital Micrograph, which outputs the number of inelastic mean free paths (IMFP) for the fluid layer and windows [16,27]. The number of IMFP's was converted to an absolute thickness by multiplying the relative measurement by the IMFP of water, which was calculated to be 50 nm (with two 50 nm thick SiN membranes) using the average atomic number formula [16,28]. Typical fluid layer thicknesses ranged from 300–800 nm for all the experiments. If different, the fluid thickness is specified.

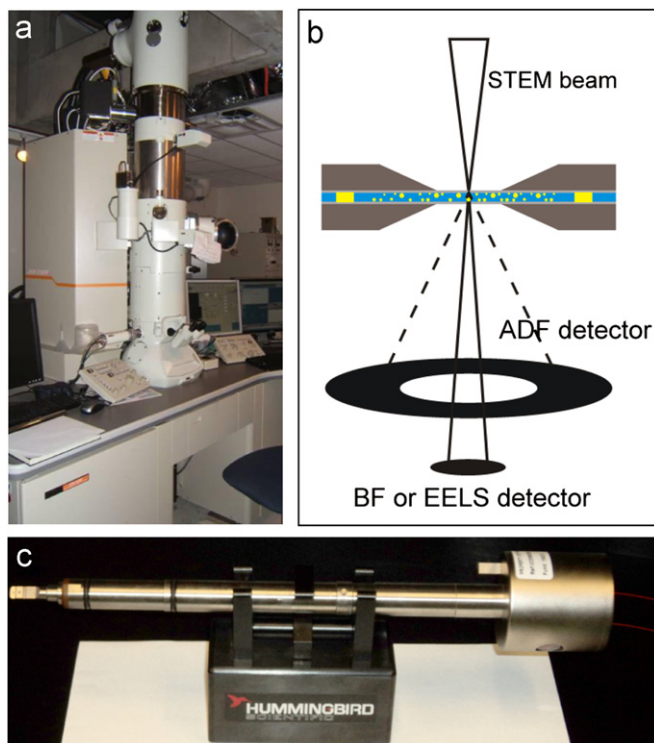


**Fig. 2.** Summary of the experimental apparatus (a) spherical aberration corrected JEOL 2100F/Cs (S)TEM (b) schematic of simultaneous ADF/BF or ADF/EELS STEM imaging and (c) Hummingbird Scientific *in situ* fluid stage holder.

Images were acquired in continuous capture mode in Digital Micrograph, such that multiple images were taken consecutively to form movies of processes in the fluid stage. The STEM beam scanned an area of  $512 \times 512$  pixels, with a pixel dwell time typically between 2–5  $\mu\text{s}$ , resulting in frame rates between 0.5–2 fps. These imaging parameters produced electron doses varying from 0.05–100 electrons/ $\text{\AA}^2$  for a single scan, for  $M=20,000$ –1,000,000. Movies were recorded with freeware software called CamStudio, and post processing and image analysis were done in ImageJ and MATLAB.

#### 2.4. Post situ analysis

To prepare the windows for *post situ* analysis, the fluid stage was disassembled after the *in situ* experiment. The windows were carefully separated using plastic tweezers, rinsed with DI water, dried, and then affixed membrane side up to an aluminum SEM stub with carbon tape (Ted Pella). The stub containing the windows was then inserted and imaged with an FEI XL30 FEG-SEM equipped with an energy dispersive x-ray spectrometer (EDS) following standard procedures.

### 3. Results and discussion

In the following sections, we discuss each observed artifact, its cause, and potential ways to mitigate the effects in detail. Artifacts discussed stem from three main sources: the experimental apparatus, direct electron beam–sample interactions, and indirect electron beam–sample interactions. We aim to elucidate the artifacts mentioned in section 1.1.1–1.2.2, more specifically the effects of surface treatment on the fluid stage windows, nanocrystal growth from solution, and the direct effect of the electron beam on freely diffusing and immobile nanoparticles.

#### 3.1. Artifacts derived from the fluid stage apparatus

##### 3.1.1. Carbon contamination

The sample preparation procedure and the physical experimental apparatus itself were both seen to be sources of artifacts due to carbon contamination. Similar to conventional STEM, carbon contamination remains a significant factor for *in situ* fluid imaging. Fig. 3a is a HAADF STEM image of contamination formed during *in situ* growth of lead sulfide crystals from an aqueous solution containing organic precursors. The bright intensity in the bottom right of the image is the corner of the SiN window, while the high intensity clusters in the background are lead sulfide crystals. The contamination is the lower intensity circular shape in the center of the image, indicated by arrows. This circular

contamination pattern is in stark contrast to the square shape of carbon contamination typically observed during imaging of solid samples with STEM. Although there is no direct evidence that this contrast change is due to carbon contamination, its low contrast is consistent with the contrast degradation observed for carbon contamination in STEM. In a separate experiment (Supplementary Movie 1), contamination forms multiple similar circular patterns much smaller than the viewing area, which rapidly nucleate and grow radially outward to cover the entire viewing area over tens of seconds. Fig. 3b shows an example of fluid stage sample contamination induced by the electron beam during a separate *in situ* lead sulfide growth experiment. The contamination formed during approximately 10 s of irradiation at  $M=150,000$ , and the image was taken directly after at  $M=80,000$ . In this case, the pattern was immobile, formed only in the area of irradiation, and remains in the image permanently.

Supplementary material related to this article can be found online at <http://dx.doi.org/10.1016/j.ultramic.2012.07.018>.

Carbon contamination is thought to be caused by mobile hydrocarbon species on the surface of the sample, which are polymerized by the electron beam to form a permanent layer of contamination [9]. For STEM the rastered area is square and thus the resulting contamination area is also square not circular. These characteristics are observed with the square contamination pattern in Fig. 3b, but Fig. 3a and Supplemental movie 1 show circular contamination patterns. The difference in the shapes of the contamination and their mobility suggests that the latter events occur inside the SiN window (adjacent to the fluid) while the former occurred on both sides of the fluid stage window. It is unclear what determines the shape of the contamination pattern, but the presence of organic species in the fluid likely leads to contamination on the fluid side of the windows, while residual carbon in the microscope and on the sample leads to contamination on the vacuum side of the windows. Additionally, the circular contamination patterns are reminiscent of a nucleation and growth process. The electron beam is likely polymerizing organic compounds in the solution at specific sites on the silicon nitride windows. After a seed is formed on the window, additional organic species adsorb to its surface and are polymerized to cause the seed to grow. It has been shown that radiolysis damage of organic crystals can also proceed by a similar nucleation and growth process [29]. In the lead sulfide experiments, isopropyl alcohol, polyvinyl alcohol, thioacetamide and lead acetate were all present in solution, and could have acted as the source for carbon contamination inside the fluid environmental chamber [8]. Thus, similar effects will likely be encountered for experiments using organic samples or solutions. Carbon contamination on the outside of the windows is likely due to the increased amount of

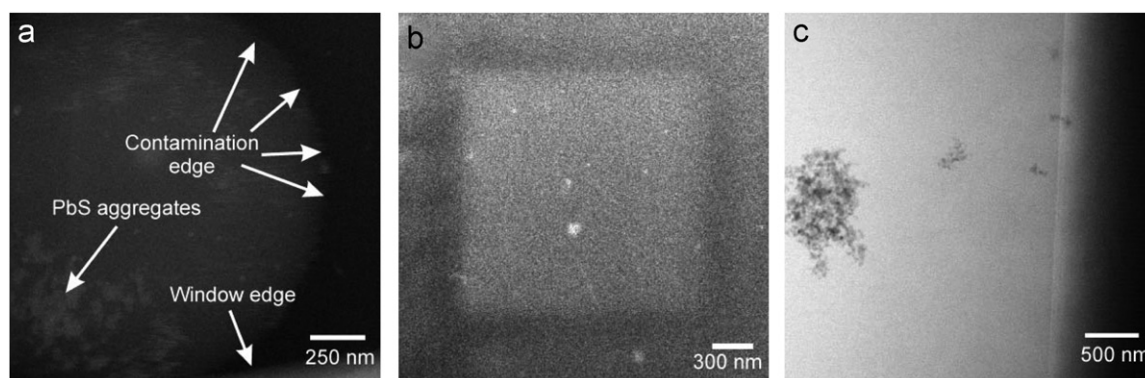


**Fig. 3.** ADF STEM images of (a) circular shaped and (b) square shaped contamination observed during an *in situ* STEM PbS crystal growth experiment (c) BF STEM image of  $\text{TiO}_2$  nanoparticles suspended in water, with all sources of carbon removed from the system.

handling the fluid stage tip and windows experience compared to a solid sample, as the fluid stage tip and windows are assembled by hand.

It is possible to eliminate all sources of carbon from a fluid sample to alleviate the contamination problems discussed. To demonstrate this,  $\text{TiO}_2$  nanoparticles suspended in DI water were imaged using stringent cleaning procedures including oxygen plasma cleaning of the windows an hour prior to the experiment, and glow discharge treatment immediately before sample loading. The fluid stage tip was also rinsed with ethanol and then DI water to remove any carbon from the surfaces. Fig. 3c is a BF STEM image from the experiment; the window edge is on the right side of the image, while the large structure on the left of the image is an aggregate of  $\text{TiO}_2$  nanoparticles. EELS confirmed the presence of a 650 nm thick fluid path between the windows in this particular area. Sustained imaging of the sample at all magnifications was possible without contamination on either side of the windows.

### 3.1.2. Membrane dewetting and surface chemistry

The surface properties of the silicon chips containing the fluid layer can also cause adverse effects in fluid stage experiments. Fig. 4 shows images of 0.1- $\mu\text{L}$  drops of DI water on SiN fluid stage chips (Hummingbird, WA, USA) subjected to two types of surface treatments, plasma cleaning and glow discharging. Images of the plasma-cleaned windows were taken directly after the treatment. There was a 10-min delay between cleaning and imaging for the glow discharge treated windows. The as made chip (Fig. 4a) is hydrophobic, with a contact angle of  $\sim 51^\circ$ , meaning the water droplet does not wet the surface well. After plasma cleaning for 1 min (Fig. 4b), the contact angle of the chip decreases to  $\sim 20^\circ$ . A similar effect is observed for glow discharge surface treatment, as well as the combination of glow discharge and plasma cleaning (Fig. 4c and d), which yielded contact angles of  $\sim 30^\circ$  and  $\sim 18^\circ$ , respectively. The contact angles were extracted from the images via standard image analysis techniques. For the case of the combined plasma and glow discharge treatment (Fig. 4d), the drop touches the edge of the window, which likely produces some error in the precise contact angle measurement; the key point however, is that the contact angle is dramatically altered by the surface treatment. The contact angle of water on chemical vapor deposited (CVD) low stress SiN, with an average surface roughness of 0.474 nm, has been shown to be  $28^\circ$  [30]. The larger contact angle of our chips is likely due to a larger SiN surface roughness and surface contamination [31,32]. Oxygen plasma cleaning acts to remove carbon contaminants from the surface and oxidize a thin layer of material on the SiN surface [31,33]. The

silicon oxide layer is further activated with hydrophilic hydroxyl groups—this effect and the removal of contaminants render the surface more hydrophilic [31]. We note that from our experiments, plasma cleaning and glow discharging do not permanently reduce the contact angle. This may be due to an “aging” mechanism, whereby the hydrophilic surface hydroxyl groups desorb with time [30]. Plasma cleaning and glow discharge, performed for a minute or less, did not cause any noticeable damage to the SiN membrane.

A hydrophobic surface is undesirable for fluid stage experiments because it can lead to dewetting of the thin film between the two windows (cf. 1.1.3). Furthermore, it is difficult to load a fluid sample onto a hydrophobic window, because the fluid would rather wet the surrounding metal surface of the fluid stage tip. Fig. 5a shows an example of a fluid front observed during STEM imaging of a dilute gold nanoparticle suspension, using untreated hydrophobic windows. This fluid front was found during imaging and was not created by the electron beam. EELS was used to confirm the presence of fluid on the right side of the image, and the absence of fluid on the left side. Furthermore, in this experiment there was not an excess of fluid in the reservoir surrounding the two silicon chips. It seems that the small amount of liquid between the two silicon chips dewetted from the surfaces and formed a visible fluid front. It is likely that the metal surface surrounding the chips pulled the fluid away from the windows, as the metal surface is more hydrophilic than the untreated SiN windows. Therefore, the tip reservoir should be filled with excess sample to ensure that dewetting of the fluid film does not occur.

Similar in nature to fluid film dewetting, bubble formation in the fluid stage limits our ability to reproducibly image fully hydrated nanomaterials *in situ*. An example of a bubble formed between the fluid stage windows is shown in Fig. 5b. The bubble

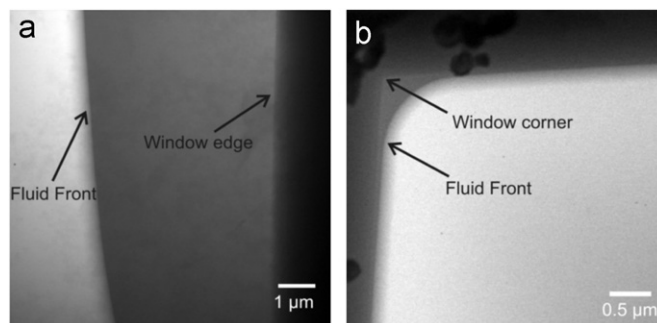


Fig. 5. (a) Fluid front observed during BF STEM imaging at  $M=200,000$ , the location of the fluid front is indicated on the image (b) bubble covering the SiN membrane during BF STEM imaging at  $M=300,000$ .

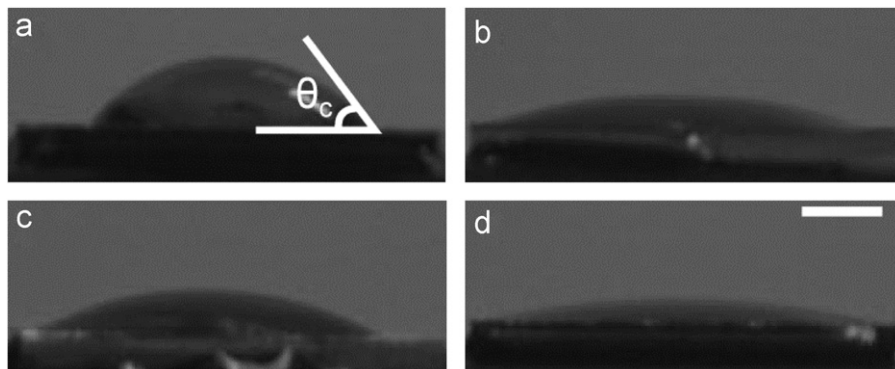


Fig. 4. Side view of a 0.1- $\mu\text{L}$  drop of DI water on a fluid stage chip (a) as-made, (b) after 1 min oxygen plasma clean, (c) after 1 min glow discharge, and (d) after 1 min plasma clean and 1 min glow discharge. The length scale for each panel is indicated by the 500  $\mu\text{m}$  scale bar in (d) and  $\theta_c$  indicates the approximate contact angle of the water drop on the chip.

formed exclusively over the electron transparent area of the SiN window, where the corner of the window is in the top left of the image and the edge of the fluid front is indicated with arrows. The bubble was present prior to imaging, as the electron beam did not have a significant effect on its size or behavior. Recently White et al. showed that nanobubbles can be formed in a fluid stage by applying current to a microelectrode immersed in the fluid to electrolyze a small amount of water [24]. The large Laplace pressure due to the curvature of the bubble should be sufficient to cause collapse of the bubble, yet it was observed that the bubble was stable [24]. Local surface properties differing from the bulk may be the cause for this inconsistency. Membrane bulging may also alter the stability of the nanobubble, as it will likely change the radius of curvature of the bubble. It is unclear from our experiments whether the bulk surface properties of the windows (*i.e.* contact angle, surface contamination, or window bulging) have a significant effect on the behavior of the system during imaging, as we have not observed systematic differences in bubble formation or dewetting with changes in the surface properties of the windows. To improve the reproducibility of future *in situ* experiments, chips from the same production batch should be treated exactly the same way prior to loading in the fluid stage, and the contact angles should be measured, as this is a common way to characterize the cleanliness of the chips [31]. Discontinuous fluid layers can be caused by particulate contamination on the windows, which can act as pinning points for liquid/solid/air interfaces in between the windows. Another possible source of bubbles between the windows is the user trapping air between the windows while loading a fluid sample. Bubble formation can be alleviated by carefully removing large particulate matter from the SiN window surface with plastic or vacuum tweezers.

### 3.2. Artifacts due to indirect electron beam sample interactions and fluid composition

The previous Section 3.1 focused on artifacts arising from various physical and chemical aspects of the experimental apparatus itself. We also observe multiple artifacts that arise from interactions between the electron beam and the fluid. These sample based interactions are of increased importance in dynamic or reactive liquid systems, because transport processes in fluids occur on much faster time scales than in solid materials. For example, diffusion coefficients for mass transport in solids are on the order of  $10^{-12}$  m<sup>2</sup>/s or smaller, whereas ionic species in water typically have diffusion coefficients on the order of  $10^{-9}$  m<sup>2</sup>/s [34]. This increased mobility in the fluid environment can lead to indirect electron beam interactions in areas not illuminated by the electron beam [8].

#### 3.2.1. Beam interactions with the fluid—crystal growth from solution

Although beneficial for nanoparticle growth experiments, the inelastic scattering of the electron beam can induce undesired crystal growth from ionic species in the fluid. Fig. 6 shows a time lapsed series of BF STEM images of crystals growing from solution on the SiN windows (*cf.* Supplementary Movie 2 for full data set). The sample imaged in this experiment was a dilute suspension of  $\sim 30$  nm gold nanoparticles in 1 mM KCl electrolyte, prepared by the Turkovich method, as described in Section 2.1. SEM/EDS showed the composition of the nanocrystals to be mainly gold, which was present in the solution in small amounts as remaining soluble precursor from the synthesis. Initially, crystal growth begins immediately once the area of interest is irradiated by the

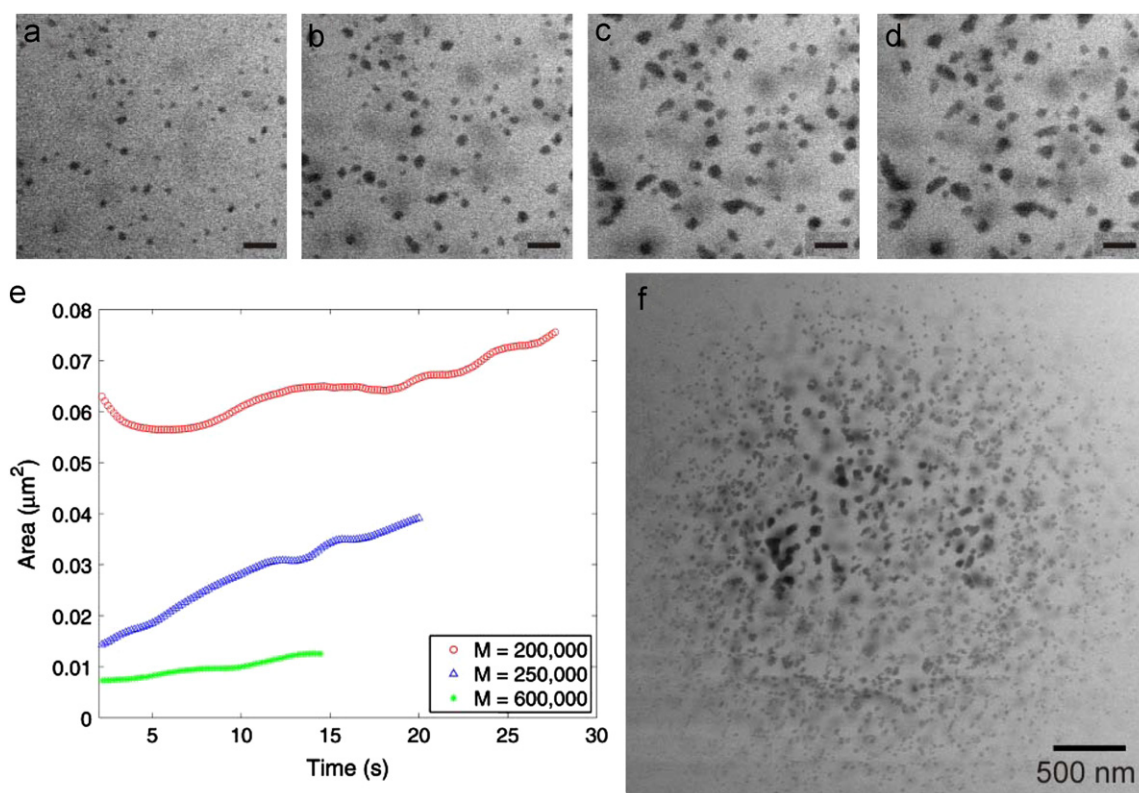


**Fig. 6.** A time lapsed series of BF STEM images of gold crystals growing on the fluid stage windows at (a)  $t=0$  s, (b)  $t=16.5$  s, (c)  $t=49.5$  s, and (d)  $t=66$  s.  $M=200,000$ , the electron dose is 3.3 electrons/(s  $\text{\AA}^2$ ), and the scale bars are 100 nm. (e) The total projected area of the crystals in focus in the image vs. time for three different magnifications. (f) BF STEM image at  $M=80,000$  of the crystal growth pattern taken after (a)–(d) with fluid still present.

electron beam at  $M=200,000$  (Fig. 6a). As the crystal growth proceeds, the crystals grow by monomer attachment and coalescence over the next minute of irradiation (Fig. 6b–d) [6]. Fig. 6e further indicates that growth has already begun in Fig. 6a and rapidly progresses to almost double the total amount of projected crystalline area in the sample. This growth was also observed at  $M=250,000$  and  $600,000$ , with similar results obtained and plotted in Fig. 6e. Out of focus shapes are also seen to grow with time in each panel of the series, suggesting that crystals were growing within the fluid cell on both the top and bottom windows. This interpretation is supported by *post situ* SEM images of both window surfaces, which revealed similar contamination patterns on each window.

Supplementary material related to this article can be found online at <http://dx.doi.org/10.1016/j.ultramic.2012.07.018>.

As discussed earlier in section 1.2.1, two of the most abundant species created during radiolysis of water by electrons are the aqueous electron and the hydrogen radical. Both species are strongly reducing and have a lifetime on the order of microseconds, which allows them to diffuse away from their origin and react. The aqueous electron has a diffusion coefficient of  $10 \times 10^{-5} \text{ cm}^2/\text{s}$ , giving it a characteristic diffusive path length of approximately  $l=300 \text{ nm}$  before it will react ( $l=(Dt)^{1/2}$ ,  $t=100 \mu\text{s}$ ) [21]. The viewing area for the time lapsed series of images was  $750 \times 800 \text{ nm}^2$ , which corresponds to the center most portion of the circular contamination pattern in Fig. 6f, where the crystals are larger and show darker contrast. The diameter of the contamination spot is approximately  $2 \mu\text{m}$ , however, suggesting that aqueous electrons were created in the irradiated area and diffused out hundreds of nanometers from the irradiated area to create the contamination pattern. This observed diffusion distance is consistent with the approximate  $300 \text{ nm}$  diffusive path length of the aqueous electron.

Similar to radiation damage observed in vitreous and biological samples, crystal growth seems to occur above a certain electron dose rate threshold. We found that this threshold is approximately  $0.5 \text{ electrons}/(\text{s} \text{ \AA}^2)$  for a  $1 \text{ mM AgNO}_3$  aqueous solution, using a pixel dwell time of  $2 \mu\text{s}$  and beam current of  $0.05 \text{ nA}$  at  $M=80,000$ . At this magnification, the smallest object that can be detected using our image analysis code is  $7 \text{ nm}$ , thus we can only conclude that the threshold electron dose we identified was for growth of nanocrystals above  $7 \text{ nm}$ . This threshold was the same for fluid path thicknesses ranging from  $400\text{--}600 \text{ nm}$  in the same cell. A more detailed study is warranted to determine the effects of precursor concentration as well as electron dose rate on the crystal growth kinetics and dose threshold.

### 3.3. Direct electron beam sample interactions

#### 3.3.1. Interactions with particles in suspension—nanoparticle repulsion

The electron beam also has a significant interaction with free nanoparticles in suspension. Fig. 7 contains a time lapsed series of images showing the expulsion of  $\text{TiO}_2$  particle aggregates from the field of view (*cf.* Supplementary Movie 3 for full dataset). As time progresses and individual clusters grow, a higher fraction of the clusters are suddenly repelled from the viewing area (Fig. 7a–d). Similar results were obtained for a dilute suspension of  $20 \text{ nm}$  gold nanoparticles (Ted Pella) (*cf.* Supplementary Movie 4). The plot in Fig. 7e reveals that initially there are 46 particle aggregates moving around the viewing area by Brownian motion, but after a time of  $\sim 10 \text{ s}$  the particles begin to leave the viewing area at a rate of approximately 1 particle/s. The particles are not observed leaving the viewing area, rather they ‘disappear’ between subsequent STEM probe scans, which are  $0.5 \text{ s}$  in duration. Because out-of-focus aggregates are not observed in the images, the aggregates are most likely being repelled in the direction perpendicular to the optical axis. Furthermore, no motion blur is observed, which indicates the aggregates are presumably moving faster than the time resolution of the STEM instrument. The initial 10-s period of constant particle number in Fig. 7e suggests a charging related phenomenon, with this initial period being the time it takes for a significant amount of charge to be acquired such that the particles are repelled from the window.

Supplementary material related to this article can be found online at <http://dx.doi.org/10.1016/j.ultramic.2012.07.018>.

Charging in the electron microscope is due to inelastic scattering of electrons, which leads to the creation and subsequent escape of secondary and Auger electrons from the sample [9,35]. In transmission microscopes, the large accelerating voltage of the incident electrons creates secondary electrons of sufficiently large energies to be transmitted through the sample, leaving an imbalance in the charge neutrality of the sample. If the sample is not conductive, there is no path for ground electrons to maintain charge neutrality, and the sample will become positively charged. With a fluid layer present, a certain fraction of the secondary electrons will also become solvated in the fluid, but most of these electrons will react in solution and not recombine with electron holes in the SiN window [21]. Transfer of electrons across the solid/liquid interface may also lead to further charging of the windows, as electrons will be able to cross the thin oxide layer on the SiN into the fluid [22].

The SiN windows, supporting silicon chips,  $\text{TiO}_2$  nanoparticles, and the water are all poor electrical conductors that will acquire

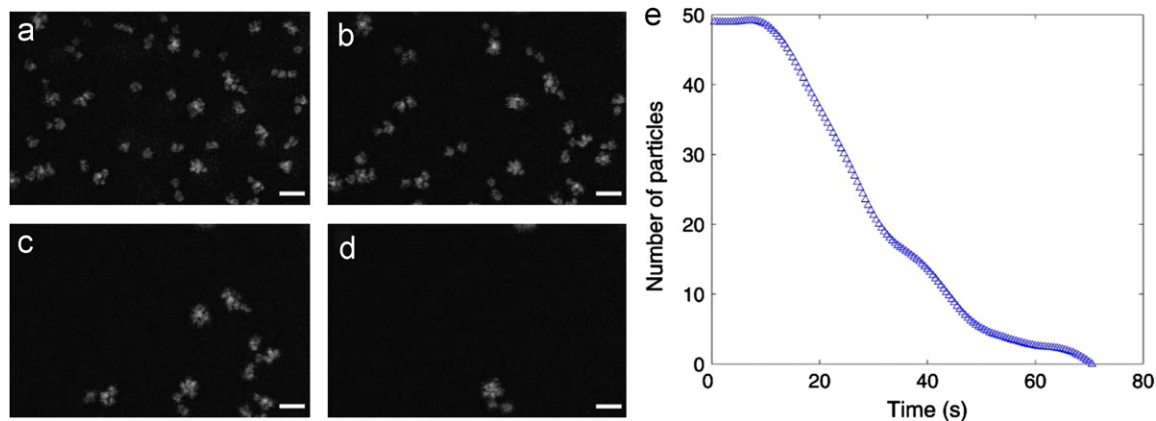


**Fig. 7.** Time lapse series of HAADF STEM images of  $\text{TiO}_2$  aggregates being expelled from the scan area at (a)  $t=0 \text{ s}$ , (b)  $t=20 \text{ s}$ , (c)  $t=40 \text{ s}$ , and (d)  $t=60 \text{ s}$ . (e) The number of aggregates as a function of time during 75 s of electron irradiation.  $M=300,000$ , the electron dose rate is  $\sim 10 \text{ electrons}/(\text{s} \text{ \AA}^2)$ , and the scale bars are  $50 \text{ nm}$ .

charge with no means of neutralizing it. Electromagnetic calculations indicate that electric fields on the order of  $10^{10}$  V/m can be established in insulating specimens subjected to TEM illumination [35]. This electric field will have a strong lateral component directed along the surface of the window, directed from the irradiated area to surrounding uncharged areas. An electric field with this orientation will repel positively charged objects from the irradiated area. This interpretation is consistent with the experimental observation that nanoparticles are being expelled from the field of view in a direction perpendicular to the optical axis, not parallel. A possible remedy for charging is to deposit a thin film of conductive material on either side of the SiN windows to provide a path for electrons to maintain electroneutrality [35]. Adding a dilute electrolyte to the solution may also help to alleviate charging, as the negatively charged ions in the solutions will be attracted to the charged window and nanoparticles to screen a fraction of the acquired charge. Care must be taken in choosing an inert electrolyte that will not react with radical species in the fluid—potassium chloride or sodium chloride are suitable electrolytes, as they are not easily reduced to solids at room temperature and will not have adverse reactions with most nanomaterials. Fluid flow can also reduce the build-up of charge in the fluid due to secondary electron production in the irradiated area [36]. This method is not very useful when imaging mobile nanomaterials because the fluid flow will carry them away from the field of view. Low dose imaging is also a potential technique to alleviate charging problems [37].

The repulsion of nanoparticles is only observed at relatively high magnifications ( $>M=300,000$ ) and electron doses ( $>10$  electrons/( $s \text{ \AA}^2$ )), but a threshold for charging has not yet been determined. Repulsion of both  $\text{TiO}_2$  and gold nanoparticles suggests that the phenomenon occurs for nanoparticles with both

positive and negative equilibrium surface charges and different intrinsic material properties (*i.e.* electrical conductivity, density, dielectric constant).

### 3.3.2. Beam interactions with nanoparticles—resolution degradation

Inelastic electron scattering can also have a significant effect on high resolution imaging inside the fluid stage. Recently 2.1 Å resolution has been demonstrated imaging PbS nanoparticles with this STEM instrument in a 300 nm layer of water [8]. Extended exposure of nanoparticles to high dose irradiation, however, seems to degrade the resolution of the image. Fig. 8a–c shows a time lapsed series of images depicting the loss of atomic resolution in a  $\text{PbO}_2$  nanoparticle attached to the SiN window, during a total irradiation time of 8 s with an electron dose of  $\sim 100$  electrons/( $s \text{ \AA}^2$ ). Initially, the nanoparticle was attached to the SiN window, which facilitated the high resolution imaging. EELS showed that there was a fluid path length of 300 nm next to the nanoparticle. Fig. 8d–f are the fast Fourier transforms (FFT) of the images directly above them. Fig. 8a clearly shows lattice fringes after 13 s of irradiation by the electron beam, confirmed by the lattice reflection marked with red in the FFT directly below (Fig. 8d). As time progresses, the atomic resolution degrades and the corresponding lattice reflection intensity in the FFT decreases (Fig. 8b and e). Approximately 8 s after Fig. 8a was acquired, lattice fringes can no longer be observed and the corresponding lattice reflection in the FFT disappears (Fig. 8c and f). Also, the particle has slightly changed orientation and an area of lighter contrast extending  $\sim 2$  nm radially from the particle surface has appeared.

Growth of contamination around the particle may be increasing the specimen density, leading to loss of resolution due to

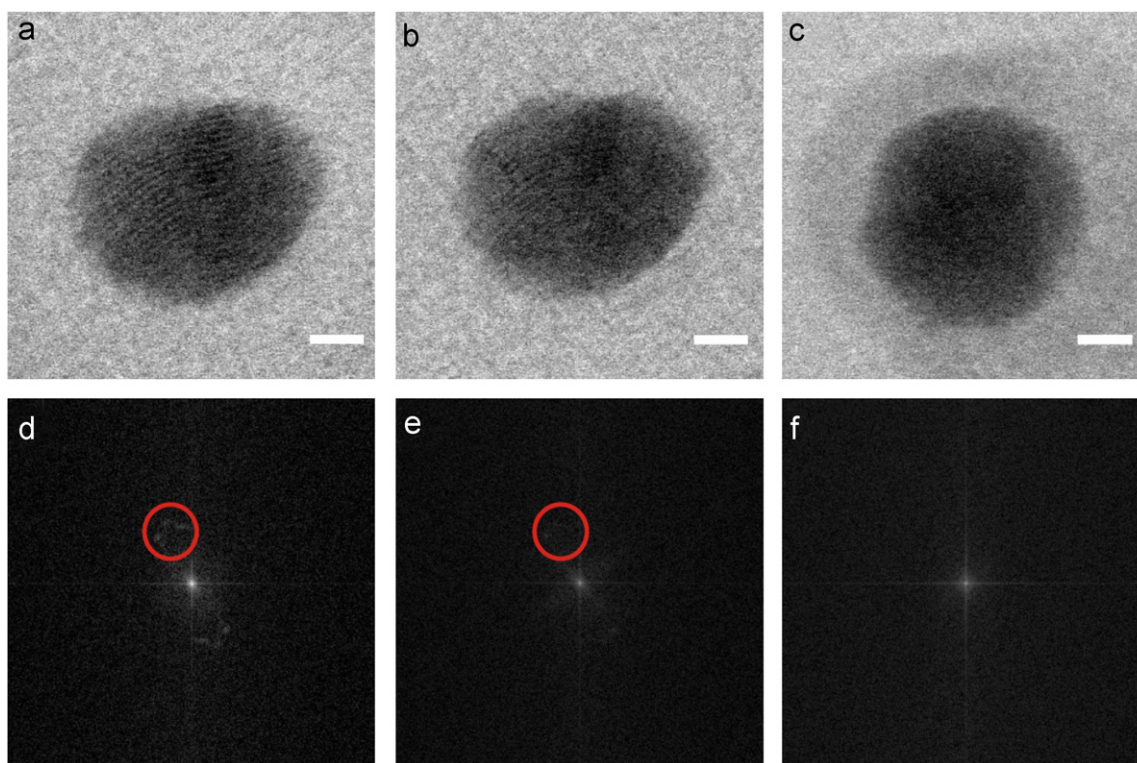


**Fig. 8.** Series of BF STEM images depicting the degradation of resolution for a  $\text{PbO}_2$  nanoparticle. The images were collected at (a)  $t=13.1$  s, (b)  $t=14.4$  s, and (c)  $t=21.0$  s, with respect to the initial irradiation of the particle. The scale bars are 2 nm, and the electron dose is  $\sim 100$  electrons/( $s \text{ \AA}^2$ ). (e)–(f) The respective Fourier transforms of the images above, the red circles in (e) and (f) highlight the lattice reflections for the nanoparticle. (For interpretation of the references to colour in this figure legend, the reader is referred to the web version of this article).

increased inelastic scattering and beam broadening. Although the nanoparticle was attached to the window, it could have changed orientation during the image acquisitions. The particle may have been dislodged by the STEM beam momentarily, allowing it to reattach to the window in a different orientation. If so, this motion may have moved the particle out of the zone axis for the lattice fringes observed, effectively degrading the resolution. Beam damage could be another source of resolution degradation, as amorphization of other nanoparticles such as mesoporous silica have also been demonstrated as occurring through a radiolysis mechanism [38]. It is unclear which mechanism is causing this phenomenon; further analysis is required to determine what is actually causing the loss of resolution with continued irradiation. Loss of resolution due to contamination can be suppressed by eliminating organic and reactive ionic species from the solution (*cf.* Section 3.1.1 and 3.2.1), while low dose imaging may be a good solution to alleviate loss of resolution in high resolution images due to electron beam damage [37].

#### 4. Conclusions

*In situ* fluid stage electron microscopy is rapidly becoming a useful tool for observing a range of different specimens encompassing biological and materials science research. As with any experimental technique, artifacts must be taken into consideration as they dictate boundaries for the types of experiments that can be performed. We described a broad summary of the artifacts and electron beam interactions that have been observed for *in situ* fluid imaging, including dewetting of fluid from the SiN windows, bubble formation, contamination, charging, and unintentional crystal growth. Loss of atomic information in high resolution images of individual nanoparticles occurred due to either radiolysis, contamination, or particle rotation. Artifacts caused by the experimental apparatus seem to arise primarily from the surface properties of the SiN windows and can be alleviated with solvent cleaning and plasma surface treatments. Plasma cleaning and glow discharge can both be used to remove residual carbon from the surface of the windows, and to render the window surfaces more hydrophilic. We showed that it is possible to eliminate carbon from a suspension of TiO<sub>2</sub> nanoparticles in water with these two treatments, and that the sample could be consistently imaged without contamination or bubbles. Meanwhile, inelastic electron scattering in the liquid layer causes a number of physical and chemical changes in the sample, creating imaging artifacts. Beam induced crystal growth is an indirect result of secondary electron formation, where some secondary electrons eventually become solvated species and reduce aqueous metallic ions to form nanocrystals. Unwanted crystal growth can be controlled by eliminating reactive aqueous ions from the solution, or imaging below the crystal growth threshold in reactive solutions. Repulsion of freely diffusing particles from the irradiated area is a consequence of secondary electrons escaping from the sample, causing charging of the SiN windows and particles in solution. This results in strong Coulombic repulsion and expulsion of nanoparticles from the scan area. Low dose imaging techniques are promising for reducing effects of both charging and beam damage in fluid samples.

#### Acknowledgments

J.E.E. and N.D.B. acknowledge NIH funding support from Grant Number 5RC1GM091755. N.D.B. acknowledges DOE funding support from Grant Number DE-FG02-03ER46057. I.A. acknowledges support from the Presidential Early Career Award for Scientists and Engineers. Support for T.J.W. was

provided by the UC Lab Fee Program and the UC Academic Senate. A portion of this work was performed at the Pacific Northwest National Laboratory which is operated by Battelle Memorial Institute for the U.S. Department of Energy under Contract No. DE-AC05-76RL01830.

#### References

- [1] M.J. Williamson, R.M. Tromp, P.M. Vereecken, R. Hull, F.M. Ross, Dynamic microscopy of nanoscale cluster growth at the solid–liquid interface, *Nature Materials* 2 (2003) 532–536.
- [2] A. Radisic, F.M. Ross, P.C. Searson, *In situ* study of the growth kinetics of individual island electrodeposition of copper, *Journal of Physical Chemistry B* 110 (2006) 7862–7868.
- [3] A. Radisic, P.M. Vereecken, J.B. Hannon, P.C. Searson, F.M. Ross, Quantifying electrochemical nucleation and growth of nanoscale clusters using real-time kinetic data, *Nano Letters* 6 (2006) 238–242.
- [4] A. Radisic, P.M. Vereecken, P.C. Searson, F.M. Ross, The morphology and nucleation kinetics of copper islands during electrodeposition, *Surface Science* 600 (2006) 1817–1826.
- [5] H.M. Zheng, S.A. Claridge, A.M. Minor, A.P. Alivisatos, U. Dahmen, Nanocrystal diffusion in a liquid thin film observed by *in situ* transmission electron microscopy, *Nano Letters* 9 (2009) 2460–2465.
- [6] H.M. Zheng, R.K. Smith, Y.W. Jun, C. Kisielowski, U. Dahmen, A.P. Alivisatos, Observation of single colloidal platinum nanocrystal growth trajectories, *Science* 324 (2009) 1309–1312.
- [7] N. de Jonge, D.B. Peckys, G.J. Kremers, D.W. Piston, Electron microscopy of whole cells in liquid with nanometer resolution, *Proceedings of the National Academy of Sciences USA* 106 (2009) 2159–2164.
- [8] J.E. Evans, K.L. Jungjohann, N.D. Browning, I. Arslan, Controlled growth of nanoparticles from solution with *in situ* liquid transmission electron microscopy, *Nano Letters* 11 (2011) 2809–2813.
- [9] R.F. Egerton, P. Li, M. Malac, Radiation damage in the TEM and SEM, *Micron* 35 (2004) 399–409.
- [10] R.M. Glaesar, in: J.I.G.J.J. Hren, D.C. Joy (Eds.), *Introduction to Analytical Electron Microscopy*, Plenum Press, New York, 1979, pp. 423–432.
- [11] W. Hobbs, in: J.I.G.J.J. Hren, D.C. Joy (Eds.), *Introduction to Analytical Electron Microscopy*, Plenum Press, New York, 1979, pp. 437–476.
- [12] K. Fukushima, M. Katoh, A. Fukami, Quantitative measurements of radiation-damage to hydrated specimens observed in a wet gas environment, *Journal of Electron Microscopy* 31 (1982) 119–126.
- [13] N. de Jonge, N. Poirier-Demers, H. Demers, D.B. Peckys, D. Drouin, Nanometer-resolution electron microscopy through micrometers-thick water layers, *Ultramicroscopy* 110 (2010) 1114–1119.
- [14] K.L. Klein, I.M. Anderson, N. De Jonge, Transmission electron microscopy with a liquid flow cell, *Journal of Microscopy* 242 (2011) 117–123.
- [15] E.A. Ring, N. de Jonge, Microfluidic system for transmission electron microscopy, *Microscopy and Microanalysis* 16 (2010) 622–629.
- [16] K. Jungjohann, J. Evans, I. Arslan, N. Browning, Electron energy loss spectroscopy for aqueous *in situ* scanning transmission electron microscopy, *Microscopy and Microanalysis* 17 (2011) 778–779.
- [17] J.M. Grogan, H.H. Bau, The nanoaquarium: a platform for *in situ* transmission electron microscopy in liquid media, *Journal of Microelectromechanical Systems* 19 (2010) 885–894.
- [18] D.B. Peckys, G.M. Veith, D.C. Joy, N. de Jonge, Nanoscale imaging of whole cells using a liquid enclosure and a scanning transmission electron microscope, *PLoS One* 4 (2009).
- [19] P.L. Gai, Development of wet environmental TEM (Wet-ETEM) for *in situ* studies of liquid-catalyzed reactions on the nanoscale, *Microscopy and Microanalysis* 8 (2002) 21–28.
- [20] A.J. Swallow (Ed.), *Radiation Chemistry: An Introduction*, Wiley Press, New York, 1973.
- [21] E.J. Hart, The hydrated electron, *Science* 146 (1964) 19–25.
- [22] S.L. Caer, Water radiolysis: influence of oxide surfaces on H<sub>2</sub> production under ionizing radiation, *Water* 3 (2011) 235–253.
- [23] R. Watanabe, K. Saito, Monte Carlo simulation of water radiolysis in oxygenated condition for monoenergetic electrons from 100 eV to 1 MeV, *Radiation Physics and Chemistry* 62 (2001) 217–228.
- [24] E.R. White, M. Mecklenburg, S.B. Singer, S. Aloni, B.C. Regan, Imaging nanobubbles in water with scanning transmission electron microscopy, *Applied Physics Express* 4 (2011).
- [25] J. Turkevich, P.C. Stevenson, J. Hillier, A study of the nucleation and growth processes in the synthesis of colloidal gold, *Discussions of the Faraday Society* (1951) 55–75.
- [26] W.B. Russel, D.A. Saville, W.R. Schowalter, *Colloidal Dispersions*, 1st ed., Cambridge University Press, Cambridge, UK, 1991.
- [27] R.F. Egerton (Ed.), *Electron Energy Loss Spectroscopy*, Plenum Press, New York, 1996.
- [28] T. Malis, S.C. Cheng, R.F. Egerton, E.E.L.S. Log-Ratio, Technique for specimen-thickness measurement in the TEM, *Journal of Electron Microscopy Technique* 8 (1988) 193–200.

- [29] J.R. Fryer, F. Holland, High resolution electron microscopy of molecular crystals. III. Radiation processes at room temperature, *Proceedings of the Royal Society A* 393 (1984) 353–369.
- [30] P. Dixit, X. Chen, J. Miao, S. Divakaran, R. Preisser, Study of surface treatment processes for improvement in the wettability of silicon-based materials used in high aspect ratio through-via copper electroplating, *Applied Surface Science* 253 (2007) 8637–8646.
- [31] H. Moriceau, Y.C.L. Tieg, F. Fournel, L.F.L. Ecarnot, S.L.E. Kerdiles, D. Delprat, C. Maleville, Direct wafer bonding surface conditioning, in: K.A. Reinhardt, R.F. Reidy (Eds.), *Handbook of Cleaning for Semiconductor Manufacturing*, Scrivener Publishing, Salem, 2011, pp. 519–529.
- [32] R.J. Hunter (Ed.), *Foundations of Colloid Science*, Oxford University Press, Oxford, 2001.
- [33] G.P. Kennedy, O. Buiu, S. Taylor, Oxidation of silicon nitride films in an oxygen plasma, *Journal of Applied Physics* 85 (1999) 3319–3326.
- [34] W.M. Deen (Ed.), *Analysis of Transport Phenomena*, Oxford University Press, New York, 1998.
- [35] J. Cazaux, Correlations between ionization radiation-damage and charging effects in transmission electron-microscopy, *Ultramicroscopy* 60 (1995) 411–425.
- [36] K.L. Liu, C.C. Wu, Y.J. Huang, H.L. Peng, H.Y. Chang, P. Chang, L. Hsu, T.R. Yew, Novel microchip for *in situ* TEM imaging of living organisms and bio-reactions in aqueous conditions, *Lab Chip* 8 (2008) 1915–1921.
- [37] J.P. Buban, Q. Ramasse, B. Gipson, N.D. Browning, H. Stahlberg, High-resolution low-dose scanning transmission electron microscopy, *Journal of Electron Microscopy* 9 (2010) 103–112.
- [38] C.F. Blanford, C.B. Carter, Electron radiation damage of MCM-41 and related materials, *Microscopy and Microanalysis* 9 (2003) 245–263.